THE EUROPEAN
PHYSICAL JOURNAL A

Regular Article – Experimental Physics

Photoproduction of η'-mesons off the deuteron

The CBELSA/TAPS Collaboration

I. Jaegle[1], T. Mertens[1], A. Fix[8], F. Huang[9], K. Nakayama[9], L. Tiator[10], A.V. Anisovich[2,3], J.C.S. Bacelar[4], B. Bantes[5], O. Bartholomy[2], D.E. Bayadilov[2,3], R. Beck[2], Y.A. Beloglazov[3], R. Castelijns[4], V. Crede[2,6], H. Dutz[5], D. Elsner[5], R. Ewald[5], F. Frommberger[5], C. Funke[2], R. Gregor[7], A.B. Gridnev[3], E. Gutz[2], W. Hillert[5], S. Höffgen[5], J. Junkersfeld[2], H. Kalinowsky[2], S. Kammer[5], V. Kleber[5], Frank Klein[5], Friedrich Klein[5], E. Klempt[2], M. Kotulla[1,7], B. Krusche[1,a], M. Lang[2], H. Löhner[4], I.V. Lopatin[3], S. Lugert[7], D. Menze[5], J.G. Messchendorp[4], V. Metag[7], V.A. Nikonov[2,3], M. Nanova[7], D.V. Novinski[2,3], R. Novotny[7], M. Ostrick[5,b], L.M. Pant[7,c], H. van Pee[2,7], M. Pfeiffer[7], A. Roy[7,d], A.V. Sarantsev[2,3], S. Schadmand[7,e], C. Schmidt[2], H. Schmieden[5], B. Schoch[5], S.V. Shende[4], V. Sokhoyan[2], A. Süle[5], V.V. Sumachev[3], T. Szczepanek[2], U. Thoma[2,7], D. Trnka[7], R. Varma[7,d], D. Walther[5], and C. Wendel[2]

[1] Department Physik, Universität Basel, Switzerland
[2] Helmholtz-Institut für Strahlen- und Kernphysik der Universität Bonn, Germany
[3] Petersburg Nuclear Physics Institute, Gatchina, Russia
[4] KVI, University of Groningen, The Netherlands
[5] Physikalisches Institut der Universität Bonn, Germany
[6] Department of Physics, Florida State University, Tallahassee, FL, USA
[7] II. Physikalisches Institut, Universität Giessen, Germany
[8] Laboratory of Mathematical Physics, Tomsk Polytechnic University, 634034 Tomsk, Russia
[9] Department of Physics and Astronomy, University of Georgia, Athens, GA 30602, USA
[10] Institut für Kernphysik, Universität Mainz, 55099 Mainz, Germany

Abstract. Quasi-free photoproduction of η'-mesons off nucleons bound in the deuteron has been measured with the combined Crystal Barrel - TAPS detector. The experiment was done at a tagged photon beam of the ELSA electron accelerator in Bonn for incident photon energies from the production threshold up to 2.5 GeV. The η'-mesons have been detected in coincidence with recoil protons and recoil neutrons. The quasi-free proton data are in good agreement with the results for free protons, indicating that nuclear effects have no significant impact. The coincidence with recoil neutrons provides the first data for the $\gamma n \to n\eta'$ reaction. In addition, also first estimates for coherent η'-production off the deuteron have been obtained. In agreement with model predictions, the total cross-section for this channel is found to be very small, at most at the level of a few nb. The data are compared to model calculations taking into account contributions from nucleon resonances and t-channel exchanges.

1 Introduction

The complex structure of the nucleon is still one of the greatest challenges for the understanding of the strong interaction in the low energy, non-perturbative regime.

---

[a] e-mail: Bernd.Krusche@unibas.ch
[b] *Present address:* University of Mainz, Germany.
[c] *On leave from:* Nuclear Physics Division, BARC, Mumbai, India.
[d] *On leave from:* Department of Physics, Indian Institute of Technology Mumbai, India.
[e] *Present address:* Institut für Kernphysik, Forschungszentrum Jülich, Germany.

One expects that, like in nuclear-structure physics, the main properties of the interaction are reflected in the excitation spectrum of the nucleon, but so far the correspondence between model predictions and experimentally observed states is quite unsatisfactory. All constituent quark models predict more states than have been observed. This problem of "missing resonances" becomes more severe the higher the excitation energy. However, the experimental data base is dominated by elastic scattering of charged pions off the nucleon, which profits from large hadronic cross-sections, but is biased against states that couple only weakly to $N\pi$. The combination of continuous wave electron accelerators with sophisticated 4π detection sys-

tems now allows the study of photon-induced reactions with at least comparable precision as hadron-induced reactions. Therefore, photoproduction of mesons has developed into a prime tool for the investigation of the nucleon excitation scheme [1,2].

Photoproduction of light mesons like pions at high incident photon energies involves many partial waves, so that the interpretation of the data requires sophisticated partial-wave analyses. Such programs are under way and will largely profit from the combination of polarized photon beams with polarized targets giving access to single- and double-polarization observables. However, alternatively due to the suppression of higher partial waves, the photoproduction of heavier mesons close to their production thresholds may give access to resonances which contribute only weakly to other channels. Photoproduction of η-mesons, which is completely dominated in the threshold region by the $S_{11}(1535)$-resonance, is the best studied example for this approach [3–19]. Since the mass of the η' ($m_{\eta'} \approx 958\,\mathrm{MeV}$ [20]) is much higher than the η-mass ($m_\eta \approx 548\,\mathrm{MeV}$ [20]), resonances contributing to η' threshold production may have masses around $2\,\mathrm{GeV}$. Of course, lower-lying resonances may also contribute due to their large widths. Because of their isoscalar nature, both, η and η' offer the additional selectivity that only $N^\star$-resonances can couple to $N\eta$, $N\eta'$. Excited Δ-states can emit these mesons only when decaying to other Δ's, in particular the $\Delta(1232)$, and thus contribute to the $\eta'\pi$-channel but not to single-η' production (again such processes have been recently intensively studied for η-production in the $\eta\pi^0$-channel [12,21–26]). Therefore, η' threshold production is expected to have a large sensitivity to $N^\star$-resonances at excitation energies, where the missing resonance problem is most severe. This is illustrated in fig. 1, where the experimentally observed nuclear excitation scheme is compared to model predictions.

Until recently, η'-photoproduction was not much explored, not even for the proton. In an early attempt, Mukhopadhyay and coworkers [27] analyzed bubble chamber data with an effective Lagrangian model and concluded that the dominant contribution comes from the excitation of a $D_{13}(2080)$-resonance. Analyses of a more recent measurement with the SAPHIR detector [28,29] claimed contributions from different resonances (S_{11}, P_{11}) and strong t-channel contributions. However, these data are not in good agreement with three later measurements with the CLAS detector at Jlab [30,17] and the Crystal Barrel/TAPS setup at ELSA [16]. These second-generation experiments, which profit from much better counting statistics and better control of systematic effects due to the use of highly efficient detector systems with large and uniform solid-angle coverage, clearly supersede the previous data. Nakayama and Haberzettl [31] presented an analysis of the earlier CLAS data in the framework of an effective Lagrangian model. They found possible contributions from S_{11}, P_{11}, P_{13}, and D_{13} resonances. However, also these results are far from being unique since the available cross-section data do not sufficiently constrain them.
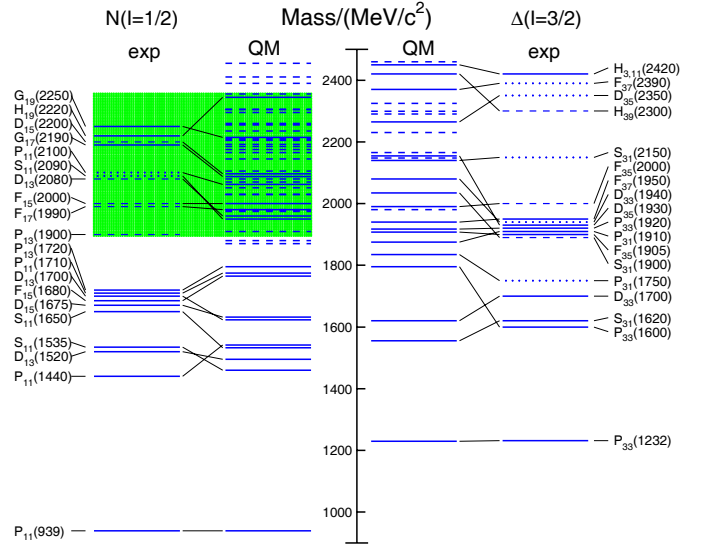

Fig. 1. (Colour on-line) Comparison of experimentally established nucleon resonances [20] (left and right) to predictions in the framework of non-relativistic quark models [32] (center). The shaded (green) area indicates the range accessible for η'-photoproduction in the present experiment.

Additional information may be obtained by exploring the iso-spin degree of freedom. The electromagnetic excitations of $N^\star$-resonances are iso-spin dependent. Resonances which are only weakly excited for the proton may give stronger signals for the neutron and vice versa. Interference patterns between different resonances and between resonances and background contributions may change due to sign changes of the electromagnetic couplings. Again, η-photoproduction with the $S_{11}(1535)$-$D_{13}(1520)$ interference [33–35] and the prominent excitation structure above the S_{11} range, which is only seen for the neutron [35–37], is a very instructive example.

Due to the technical problems involved in the measurement of small production cross-sections off bound nucleons, photoproduction of η'-mesons off the neutron had not been studied up to now. Here, we report the first results for quasi-free η'-photoproduction off protons and neutrons bound in the deuteron. The paper is organized in the following way. Sections 2 and 3 summarize the experimental setup and the data analysis. The bases of the models the data are compared to are discussed in sect. 4. The results are summarized in sect. 5. First, the data in coincidence with recoil protons are compared to free proton data as a check of the quasi-free production hypothesis. Both, quasi-free proton and neutron data are then compared to model fits. In addition to the quasi-free data, a first estimate for the cross-section of the coherent process $\gamma d \to d\eta'$ was extracted. Final conclusions are given in sect. 6.

2 Experimental setup

The experiment was done at the electron stretcher accelerator ELSA in Bonn [38,39]. For the measurements discussed here, electron beam energies of $2.6\,\mathrm{GeV}$ and
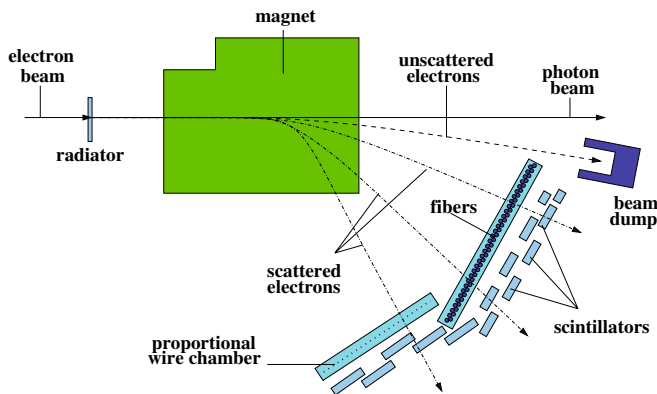
Fig. 2. Setup of the tagging spectrometer.

Table 1. Summary of beam times. E_{e^-}: electron beam energy, E_{γ_t}: maximum energy of tagged photons, E_{pol}: energy of maximum linear photon beam polarization, Φ_0: energy integrated electron flux. Total lifetime: beam time multiplied by acquisition lifetime.

Characteristics	A	B	C	D	E
E_{e^-} [GeV]	2.6	2.6	3.2	3.2	3.2
E_{γ_t} [GeV]	2.0	2.0	2.5	2.5	2.5
E_{pol} [GeV]	1.0	1.0	unpol.	1.2	1.6
Total lifetime [h]	138	18	189	25	25
Φ_0 [$10^7 e^-$/s]	1.75	1.6	1.6	2.8	2.8

3.2 GeV have been used. Real photons were produced with the bremsstrahlung technique. Their energies were tagged via the momentum analysis of the scattered electrons by a magnetic spectrometer, which is schematically shown in fig. 2 (see [40] for details). For this experiment only the part of the focal plane covered by the scintillating fiber detector but not the part covered by the proportional wire chamber was used. This limited the maximum tagged photon energies to 80% of the electron beam energy. The different beam settings are summarized in table 1.

Due to these settings and the typical $1/E_\gamma$ intensity distribution of the photon flux, the average time integrated flux at photon energies above 2 GeV was roughly lower by a factor of two than the flux at lower energies. The largest part of the 3.2 GeV beam time was done with a copper radiator foil of 0.3% radiation lengths thickness, producing unpolarized bremsstrahlung. For a small part of this beam time and for the running with the 2.6 GeV electron energy a diamond radiator was used to produce a linearly polarized photon beam via coherent bremsstrahlung (see [41] for details about linear polarization) for the extraction of photon beam asymmetries. However, the statistical quality of this observable was marginal for η'-production, since for most of the beam time the setting of the polarization peak was optimized for η-production at lower incident photon energies (see table 1). Therefore photon asymmetries have not been analyzed for the η'-channel.

The target consisted of a vertically mounted cryostat attached to a tube entering the Crystal Barrel detector from the upstream side. The target cell itself was a capton cylinder (0.125 mm foil thickness) with a diameter of 3 cm and a length of 5.3 cm, filled with liquid deuterium (surface thickness 0.26 nuclei/barn). The reaction products emerging from the target were detected with electromagnetic calorimeters covering almost the full solid angle; the Crystal Barrel (CB) detector (1290 CsI crystals covered the full azimuthal angle for polar angles between 30° and 168°) [42] and the TAPS detector (528 BaF$_2$ crystals mounted as hexagonal forward-wall covered polar angles down to 4.5°) [43,44]. Plastic scintillator detectors in front of the TAPS modules and a scintillating fiber detector [45] inside the Barrel covering the same polar-angle range were used for charged-particle identification. A schematic view of the full arrangement is shown in fig. 3, more details can be found in [40], where apart from the target an identical setup was used. The time-of-flight walls were mounted but not used for this experiment.

The first-level hardware trigger for the experiment was exclusively based on signals from the TAPS forward-wall detector. The reason is that the CB was read out by photodiodes without timing information. Measurements of reactions off the free proton can use signals from recoil protons traversing the inner detector. However, in order to have an identical trigger setting for quasi-free production off the proton and off the neutron this option was not used. The modules of the TAPS detector were equipped with two independent leading edge discriminators, combined in two different ways into logical groups (see fig. 4). For most of them (rings 12–5 from outer edge to center) the lower threshold was set to ≈ 55 MeV (LED-low). It was set to 80 MeV, 135 MeV, 270 MeV for rings 4, 3, 2, respectively. The innermost ring was not allowed to trigger. The LED-high thresholds were set to 70 MeV for rings 9–7, rising from 105 MeV (ring 6) to 180 MeV (ring 2). Again, the innermost ring was not allowed to trigger and the three outer rings (block G) had no LED-high. The first-level trigger included two components: one or more LED-low discriminators from at least two logical sections above threshold or at least one LED-high discriminator above threshold. In the second case, a second-level trigger from the FAst Cluster Encoder (FACE) of the Crystal Barrel, indicating at least two separated hits in the Barrel, was required in addition. All first-level triggers thus required detection of at least one photon in TAPS. Such a trigger is only efficient for reactions with a high multiplicity of photons like the $\eta' \to \pi^0\pi^0\eta \to 6\gamma$ or the $\eta \to 3\pi^0 \to 6\gamma$ decays. But even then the trigger efficiency for mesons at backward angles is not large. In principle, also events where a recoil nucleon is detected in TAPS might activate the hardware trigger. This would, however, lead to uncontrollable trigger efficiencies since the LED thresholds are only calibrated for photons (recoil nucleons have different signal shapes in BaF$_2$ scintillators) and the energy deposited by neutrons is more or less random. Therefore only events where photons alone (identified by non-firing veto detectors and time-of-flight *versus* energy) fulfilled the first-level trigger conditions were accepted in the analysis.
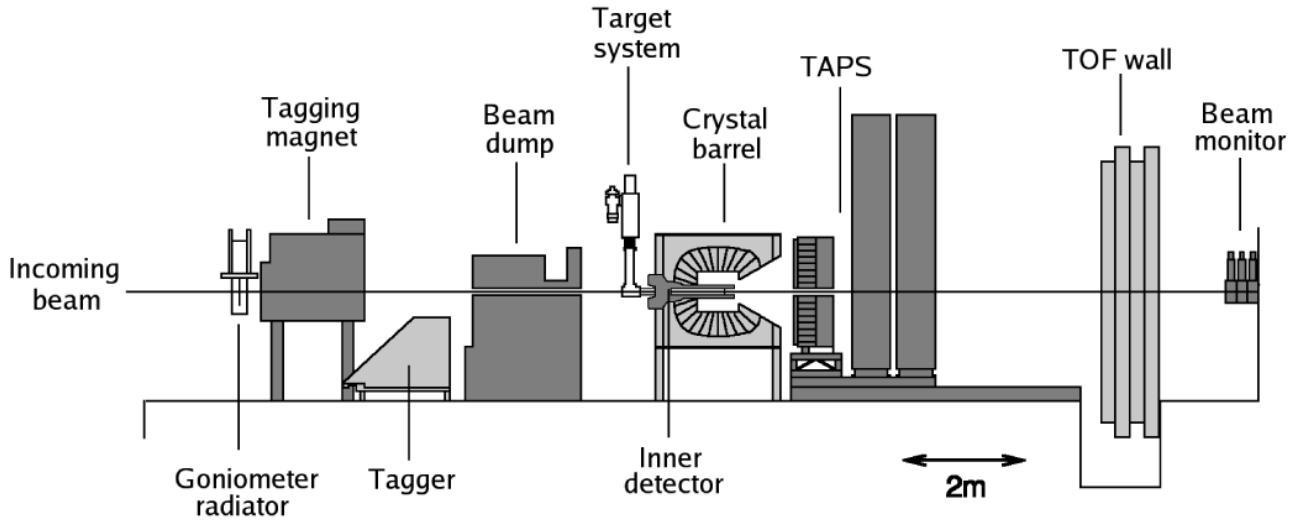
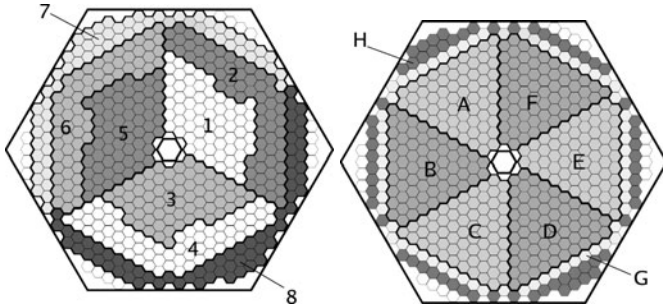**Fig. 3.** Overview of the experimental setup at the ELSA accelerator.

Fig. 4. Front view of the TAPS forward wall. Left-hand side: logical segmentation for the LED-low trigger, right-hand side: logical segmentation for the LED-high trigger (see text).

3 Data analysis

3.1 Particle and reaction identification and extraction of cross-sections

Photoproduction of η'-mesons was identified via the $\eta' \to \eta\pi^0\pi^0 \to 6\gamma$ decay chain, which has a branching ratio of 8%. Cross-sections were extracted for four different reaction types. The two most important ones are quasi-free production off the proton $\gamma d \to (n)p\eta'$, which requires co-incident detection of an η' and a recoil proton and quasi-free production off the neutron $\gamma d \to n(p)\eta'$ via detection of the η' together with a recoil neutron. For the control of systematic uncertainties (see below) also the inclusive reaction $\gamma d \to (np)\eta'$ with no condition for recoil nucleons was analyzed. Finally, also an estimate of the fully inclusive reaction $\gamma d \to X\eta'$ was obtained, where also final states like $\eta'\pi$ contribute.

In the first step of the analysis photon and neutron candidates (called "neutral hits") were separated from proton candidates (called "charged hits"). This was done in the CB with the help of the scintillating fiber detector and in TAPS with the charged-particle veto detectors. In

TAPS a hit was assigned to "charged" if the veto of any cluster module or the veto of any neighbor of the central module of the cluster had responded (even if the neighbor module itself had no signal above threshold). The latter condition applies to charged particles which traverse the edge of a veto but deposit their energy in the neighbor module (due to large impact angles). All other hits were assigned to "neutral". In the Barrel, a hit was assigned to "charged", if at least two layers of the inner detector had recorded a hit within $\pm 10°$ of azimuthal angle. It was assigned to "neutral" if no layer had fired within this azimuthal angle. Hits with one responding layer of the inner detector were discarded. In the TAPS forward wall, correct identification of protons, neutrons, and photons can be additionally controlled with a time-of-flight *versus* energy analysis, while in the CB no direct separation of photons and neutrons is possible (more details on particle identification are given in [40] (CB) and [46] (TAPS)).

In the next step, events with at least six "neutral" hits as candidates for the η'-decay photons were selected and assigned to four partly overlapping classes corresponding to the above-defined reaction types: six "neutral" and one "charged" hit for the $(n)p\eta'$ final state, seven "neutral" for the $n(p)\eta'$ final state, six or seven neutral or six neutral and one charged for $(np)\eta'$, and at least six "neutral" without any further condition for $X\eta'$.

The identification of the $\eta'N$ final states was then based on a combined invariant- and missing-mass analysis. The invariant-mass analysis identified the η', the missing-mass analysis excluded events where further mesons have been produced but have escaped detection (except for the $X\eta'$ final state where such events were included).

The invariant mass of all possible disjunct photon pairs was calculated. Only events having at least one combination of six "neutral" hits to two photon pairs with invariant masses between 110 and 160 MeV (pions) and one pair between 500 and 600 MeV (η) were kept. In cases where the photons could be combined in more than one way to

fulfill this condition, the "best" combination was chosen via a χ^2 minimization:

$$\chi^2 = \sum_{k=1}^{3} \frac{(m_k(\gamma\gamma) - M_k)^2}{(\Delta m_k(\gamma\gamma))^2} , \qquad (1)$$

where for each disjunct combination of the six photons into three pairs the invariant masses are ordered so that $m_1(\gamma\gamma) \leq m_2(\gamma\gamma) \leq m_3(\gamma\gamma)$. The $\Delta m_k(\gamma\gamma)$ are their uncertainties (computed event-by-event from the detector resolution for energies and angles) and M_k is the π^0-mass for $k = 1, 2$ and the η-mass for $k = 3$. The above case applies to events with exactly six "neutral" hits, where in total 15 different combinations are possible (events with recoil proton or without detected recoil nucleon). For candidates for the quasi-free reaction off the neutron (seven "neutral" hits) one must in addition loop over the unpaired hit, since in CB photons and neutrons cannot be distinguished. This corresponds at maximum to 105 combinations, giving rise to larger combinatorial background. In this case, the hit which was not assigned to a pion- or η-decay photon is accepted as neutron candidate. In the case of the $X\eta'$ final state even higher multiplicities may occur.

As in [40] the nominal masses of the mesons were then used as a constraint to improve the experimental resolution by re-calculating the measured photon energies from

$$E'_{1,2} = E_{1,2} \frac{m_{\pi^0,\eta}}{m_{\gamma\gamma}} , \qquad (2)$$

where $E_{1,2}$ are the measured photon energies, $E'_{1,2}$ the re-calculated, $m_{\pi^0,\eta}$ are the nominal π^0, η masses, and $m_{\gamma\gamma}$ the measured invariant mass.

The obtained 6-photon invariant-mass distributions using the re-calculated γ-energies are shown in fig. 5, (left column) for the inclusive reaction $(np)\eta'$ and in coincidence with recoil protons $(n)p\eta'$ and neutrons $(p)n\eta'$. In all cases a clear peak is visible at the nominal η'-mass of 958 MeV. The shape of the invariant-mass peaks has been generated via a Monte Carlo simulation with the GEANT package [47] and fitted to the data together with a background polynomial. The peak-to-background is best for $(n)p\eta'$, intermediate for $(np)\eta'$, and worst for $(p)n\eta'$. This is as expected from the above discussion: events with seven "neutral" hits have a much larger chance for combinatorial background (for example from $\eta\pi^0$, $\eta'\pi^0$, ηn final states, when a photon is falsely assigned as neutron or vice versa) than events with six "neutral" and one "charged" hit. This is also reflected in the background of the missing-mass spectra, which is much more pronounced when the invariant-mass background is not subtracted (compare center and right column in fig. 5).

For the missing-mass analysis the recoil nucleons were treated as missing particles, no matter if they were detected or not. The missing mass Δm of the reaction was calculated for quasi-free production of η'-mesons off nucleons via:

$$\Delta m = |\mathbf{P}_\gamma + \mathbf{P}_N - \mathbf{P}_{\eta'}| - m_N, \qquad (3)$$
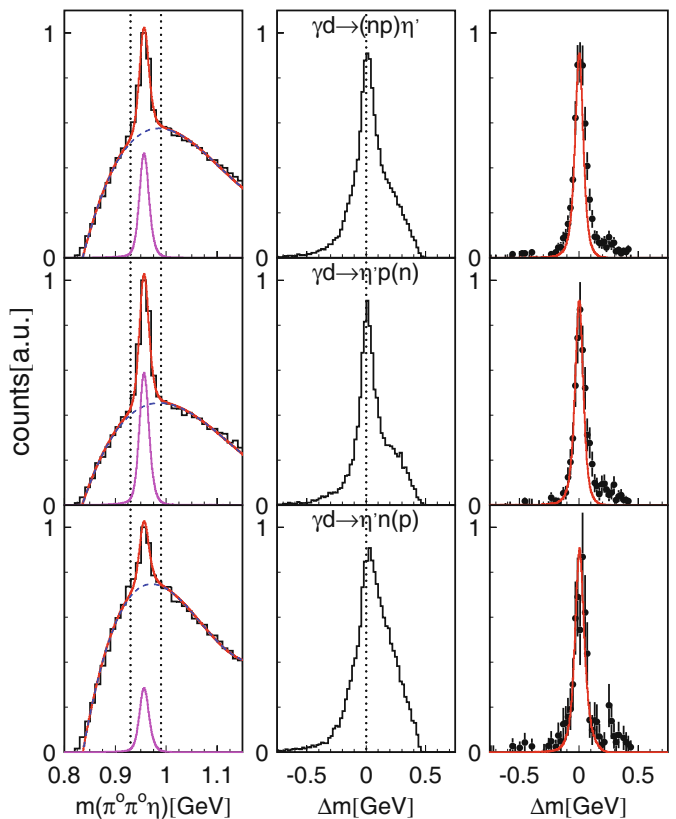
Fig. 5. (Colour on-line) Top to bottom: reactions $\gamma d \to (np)\eta'$, $\gamma d \to p(n)\eta'$, $\gamma d \to n(p)\eta'$. Left-hand side: 6γ invariant-mass spectra, dashed (blue) curves: background fit, solid (red) histograms: sum of background and η'-peaks, in addition: simulated line shapes (pink solid lines). Center: missing-mass spectra for cut on η' invariant-mass peaks; right-hand side: (black) points: missing-mass spectra for events in invariant-mass peak after background subtraction, solid (red) curves: simulated line shapes. All spectra for incident photon energies from threshold to 2 GeV (integrated over all beam times and the full polar-angle range).

where $\mathbf{P}_\gamma$, $\mathbf{P}_N$, $\mathbf{P}_{\eta'}$ are the four-momenta of the incident photon, the incident nucleon (assumed to be at rest), and the produced η'-meson; m_N is the nucleon mass. The resulting distributions peak around zero for quasi-free η'-production and are somewhat broadened by the momentum distribution of the bound nucleons, which was neglected. The distributions are shown in fig. 5, center column. They have been constructed for an invariant-mass window from 930–990 MeV (see fig. 5, left column). Since the background cannot be completely removed by cuts on invariant mass and missing mass, in the final step the invariant-mass spectra have been analyzed (*i.e.* fitted by line shape and background) for each bin of missing mass. The resulting missing-mass spectra corresponding to the invariant-mass peaks are shown in fig. 5, right-hand side. Background is much reduced and the shapes of the missing-mass peaks are quite well reproduced by the Monte Carlo simulation. The residual background at positive missing masses is mainly due to the $\eta'\pi$ final state,
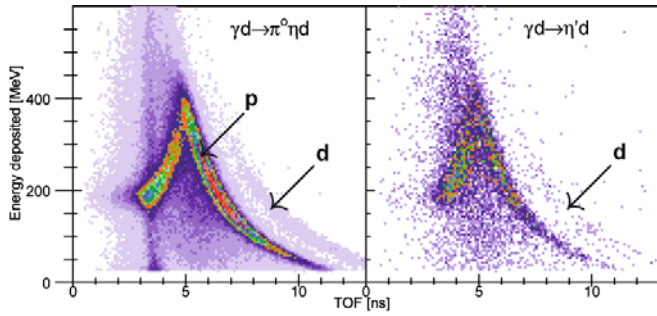
Fig. 6. Time-of-flight *versus* energy for charged particles in TAPS under the condition of invariant-mass signals (cuts on invariant-mass peaks, no background subtraction) for the $\pi^0\eta$-channel (left-hand side), and the η'-channel (right-hand side). The prominent band corresponds to protons, the less prominent band to deuterons.

from events where the pion escaped detection. It becomes more important at incident photon energies above 1.6 GeV (see also fig. 8 in sect. 5.1) and extends into the range of the missing-mass peak. This explains also the deviation of the simulated line shape from the data at positive missing mass. Therefore at energies above 1.6 GeV only events with missing mass between -200 and 0 MeV were accepted. This reduces counting statistics by a factor of two but guarantees negligible background contamination. The analysis described above was done independently for each bin of incident photon energy and η' polar angle.

Absolute cross-sections were derived from the target density, the incident photon flux, the decay branching ratio, the detection efficiency for the $\eta' \rightarrow 6\gamma$ decay, and the detection efficiency for recoil nucleons. The detection efficiency was determined via Monte Carlo simulations using the GEANT3 package [47], which included all features of the detector system and all software cuts for particle and reaction identification. Events for the final states $(np)\eta'$, $(p)n\eta'$, and $(n)p\eta'$ were generated evenly distributed in phase-space including the effects of nuclear Fermi motion, tracked with the GEANT package, and analyzed in the same way as the experimental data. The tracking of recoil nucleons was done with the GEANT-CALOR program package [48], which is optimized for hadronic interactions from a few MeV to several GeV range, including the interactions of low-energy neutrons. The efficiency correction was then done in the usual way as a function of the incident photon energy and meson cm polar angle.

Finally, an estimate of the cross-section for the coherent reaction $\gamma d \rightarrow \eta' d$ was extracted in the following way. Deuterons in the TAPS detector can be identified via a time-of-flight *versus* energy analysis (time-of-flight path 1.18 m) as shown in fig. 6, where only charged hits (identified by the veto detectors) are included. The distribution at the right-hand side of fig. 6 is obtained for 6-photon events with an invariant mass corresponding to the η'-meson. The left-hand side of the figure shows for comparison the result for the $\eta\pi^0$-channel, which shows a much more pronounced deuteron band since it has a larger coherent component. Events can then be selected by a cut on
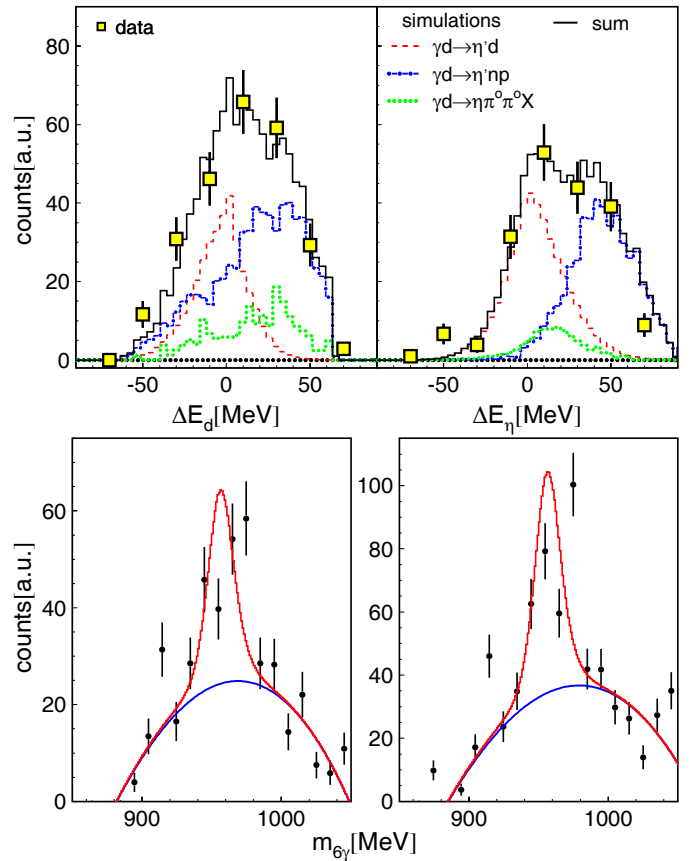
Fig. 7. Upper part: missing energy. Left-hand side: deuteron missing energy; right-hand side: η' missing energy after cut on the deuteron missing energy between ± 35 MeV. Points: data, histograms: simulation of signal and background shapes. Bottom part: invariant-mass spectra. Cut on the deuteron missing energy ± 35 MeV, cut on the η' missing energy: ± 25 MeV (left-hand side), ± 50 MeV (right-hand side). Points: data, fitted with background polynomial plus simulated line shape.

the deuteron band, which gives a quite clean data sample for the $d\eta'$ final state.

However, due to kinematic reasons (mesons from the coherent reaction are mostly emitted to forward angles due to the nuclear form factor) most deuterons are emitted into the solid angle of the Barrel, where they cannot be identified via time-of-flight. Therefore a more complicated analysis based on reaction kinematics was necessary. The major steps are summarized in fig. 7. For deuterons in the Crystal Barrel, first the inner detector was used for charged-particle identification and it was required that the deuteron candidate was co-planar with the η'-meson. Further exploiting the two-body kinematics of the final state, the cm-energies (photon-deuteron center-of-momentum system) derived from the final-state four-vectors were compared to the respective values calculated from the incident photon energy for the deuteron (deuteron missing energy) and for the η' (η' missing energy). These spectra are compared in fig. 7, upper part to Monte Carlo simulations of the coherent and breakup process and of residual background from $\eta\pi^0\pi^0$ phase

space contributions not related to η'-production. The corresponding invariant-mass spectra after more or less stringent cuts on missing energy are shown in the bottom part of fig. 7. The final signal strength was then extracted via a fit of a background polynomial and the simulated invariant-mass line shape to the data. The systematic uncertainty of this procedure was estimated by a variation of the η' missing energy cut (± 50 MeV, ± 25 MeV, -50 MeV– 0 MeV). The first cut cannot completely suppress incoherent background, results from the most stringent, asymmetrical cut are unfortunately limited by the statistical quality of the data.

3.2 Systematic uncertainties

Due to the small cross-section of η'-production, the requirement of coincident detection of the mesons with recoil particles, and the low trigger efficiency (only trigger signals from photons in TAPS) counting statistics were low. Therefore statistical uncertainties were rather large (on the order of 15–35% for the $(p)n\eta'$ final state), which makes it difficult to investigate systematic effects hidden in statistical fluctuations. Therefore, systematic uncertainties were partly extracted from other reaction channels, in particular from the $\eta \to 6\gamma$ channel.

Three different types of systematic uncertainties may effect the quasi-free cross-sections: overall uncertainties which cancel exactly in the comparison of proton and neutron final state, uncertainties with similar effects, which cancel to a large extent in ratios, and uncertainties related to specific final states which do not cancel.

Into the first category fall the systematic uncertainty of the incident photon flux, the uncertainty in target thickness (as well as effects from possible slight misplacements of the target), and the uncertainty from the η' decay branching ratios. An estimate of the flux uncertainty was obtained by a comparison of η-photoproduction [35] cross-sections obtained by a separate analysis of beam times (A) and (C) (see table 1). These two beam times used different incident electron beam energies, so that the same photon beam energies were mapped to different sections on the focal-plane detector. Furthermore, since (C) was using an unpolarized beam and (A) linear polarization, also the energy dependence of the flux was different due to the coherent peak at roughly 1 GeV. Typical deviations between the η cross-sections produced from these two beam times are at the 5% level, maximum deviations around 10%. Since the results from both beam times (with approximately equal statistical weight) were averaged, we estimate the systematic flux uncertainty at 10%. The overall systematic uncertainty coming from target thickness and positioning is on the order of a few per cent. The systematic uncertainty of the branching ratios for $\eta' \to \eta\pi^0\pi^0 \to 6\gamma$ is around 7%. Allowing for some cancellation, we estimate a total normalization uncertainty of $\approx 15\%$. A comparison of the results for quasi-free production off the proton to free proton results for both the η- and the η'-channel (see below) did not reveal discrepancies beyond this level.

The second class of systematic uncertainties is dominated by the uncertainty of the η' identification by the missing-mass and invariant-mass analysis and the simulation of the η' detection efficiency, which are of course related (the better the respective cuts are reflected by the simulation the smaller the uncertainty). The simulation of the detection efficiency of photons followed by an invariant-mass analysis for meson identification is very well under control for the CB/TAPS setup. This has been tested for example via a comparison of the results for the $\gamma p \to p\eta$ reaction obtained from the analysis of the $\eta \to 2\gamma$ and $\eta \to 6\gamma$ decay channels [11,13,16]. Agreement with the PDG value of the $\Gamma_{\eta \to 3\pi^0}/\Gamma_{\eta \to 2\gamma}$ ratio is reported in [13] within an uncertainty at the 2% level. Since errors for the $\eta \to 2\gamma$ channel in photon detection or invariant-mass analysis enter cubed into the $\eta \to 3\pi^0$ channel, this sets stringent limits on the uncertainty. Already a 2% error in photon detection efficiency would result in an 8% deviation between the two decay channels.

A further uncertainty is related to the choice of the event generator used for the simulation. Events were generated evenly distributed in phase-space, where the effects of Fermi motion were modeled using the deuteron wave function in momentum space from [49]. Since the correction was done as a function of the incident photon energy and cm polar angle of the η', the angular distribution of the η'-mesons itself is not critical. However, deviations could arise if for example final-state interaction effects modify the correlation between meson polar angle and kinetic energy or between meson polar angle and the kinematic variables of the recoil nucleon. Possible systematic effects of this kind were investigated with a different simulation, where the detection efficiency for η'-mesons $\epsilon(T_{\eta'}, \Theta_{\eta'})$ and the detection efficiency for recoil nucleons $\epsilon(T_N, \Theta_N)$, $N = n, p$ was quasi-factorized and parameterized in dependence on laboratory kinetic energies $T_{\eta'}$, T_N and polar angles $\Theta_{\eta'}$, Θ_N of the particles. Typical efficiencies are 10% for η' detection (including trigger efficiency), 95% for protons, and 10–30% for neutrons (depending on energy and including the identification of the neutron). These kinematic observables can be directly extracted from the measured data (the neutron kinetic energy is extracted via the over determined reaction kinematic from the incident photon energy, the measured η' four-vector and the measured neutron angles). Therefore, an event-by-event efficiency correction with the product $\epsilon(T_{\eta'}, \Theta_{\eta'}) \cdot \epsilon(T_N, \Theta_N)$ becomes possible, which does not rely on any model assumptions about the kinematic final-state variables. This efficiency correction does, however, not include the missing-mass cut, which depends on incident photon energy. A correction for this effect was extracted from a phase-space simulation. It does not much depend on details of the event generator, since it uses only the ratio of two different analyses (with and without missing-mass cut) of the same simulation. Actually as expected from fig. 5 the correction factor is close to 2 for a cut from -200 MeV to 0 (left half of the peak). The results from the two different detection efficiency simulations agreed to better than 5% for all investigated reaction channels, and we assume a systematic uncertainty in this range.

The effects from the background under the invariant-mass peaks (see fig. 5), which is more important for the neutron channel, have not been treated as independent systematic uncertainties, they have been included via the peak-background separation into the statistical uncertainties. An additional systematic uncertainty could arise from the missing-mass analysis. Variations of the accepted missing-mass range show significant influence on the extracted cross-section. This, however, does not seem to be a problem of the agreement between simulation and data, since the shapes of the signals agree well at the left-hand side of the peaks, but start to disagree at the right-hand side where background from $\eta'\pi$ final states is expected. Therefore, for incident photon energies above 1.6 GeV only events with $\Delta m < 0$ have been accepted. However, we assign an additional uncertainty rising from 3% at threshold ($\eta\pi$ background starts to contribute above 1.6 GeV) to 10% at the maximum energy. Altogether, independent on the reaction channel, we estimate an uncertainty of 6% close to threshold up to 12% at the highest incident photon energies (not including effects of recoil nucleon detection).

The last class of uncertainties are those related to the detection of recoil nucleons, which will not cancel in the comparison of neutron-proton cross-section ratios. The detection of the recoil nucleons was included in the simulations using the GCALOR package [48], which is optimized for this purpose. For the proton, the quality of this simulation could be cross-checked with experimental data for the $\gamma p \rightarrow p\eta$ and $\gamma p \rightarrow p\pi^0\pi^0$ reactions which have been measured with the same setup. The proton detection efficiency was simply determined as ratio of the number of events with detected recoil proton to the total number of events from these reactions. The efficiencies have then also been simulated and the simulated and measured values agree within 8% for slow protons and 4% for fast protons. Combining all uncertainties except the overall normalization we estimate for the quasi-free proton channel 10% at threshold rising to 15% at 2.5 GeV.

For the neutron detection efficiency there are no direct measurements with the combined TAPS/CB setup in Bonn. For the TAPS detector it had been experimentally determined from the $\gamma p \rightarrow n\pi^0\pi^+$ reaction at the MAMI accelerator in Mainz [50]. The results are consistent with the GCALOR simulation, when the conditions of the Mainz setup are used ($T_n = 250$ MeV: simulated 18.5%, from data 19.1%). The neutron detection efficiency of the CB was measured at the LEAR ring at CERN [51]. Results from the present GCALOR simulation are in good agreement with the LEAR result except for slow neutrons ($T_n < 75$ MeV), where the efficiency is very dependent on detector thresholds and the neutron kinetic energy. However, in any case it is necessary to determine "effective" neutron efficiencies which take into account the identification of the neutrons out of at least seven neutral hits via the invariant-mass analysis discussed in sect. 3.1. This could only be done by simulations. The reduction of the efficiency under this conditions compared to the situation were only neutrons are simulated is substantial, of the order of 25%–35%. We therefore estimate the absolute systematic uncertainty for neutron detection at the

Table 2. Summary of systematic uncertainties for the quasi-free reactions. [1] Photon flux, target thickness, decay branching ratios; [2] trigger efficiency, η' analysis cuts, η' detection efficiency. When two numbers are given the first corresponds to threshold, the second to $E_\gamma = 2.5$ GeV, and linear interpolation.

Source	$\gamma d \rightarrow (n)p\eta'$	$\gamma d \rightarrow (p)n\eta'$
Overall normalization[1]	15%	15%
η' detection[2]	6%–12%	6%–12%
Recoil nucleon detection	8%–4%	15%
Total except overall norm.	10%–15%	16%–20%

15% level. Altogether a systematic uncertainty of 16% at reaction threshold up to 20% at highest incident photon energies is estimated for the quasi-free neutron channel (excluding the overall normalization uncertainty).

A further systematic uncertainty could arise from the misidentification of recoil nucleons. While the loss of events is included in the simulated efficiencies, misidentified protons might contaminate the neutron sample or vice versa, where the first problem is more severe, due to the smaller absolute detection efficiency for neutrons. The properties of the inner detector for proton identification have been studied in detail in [45] with simulations and data from the reaction $\gamma p \rightarrow \pi^0 p$. The main result was that the average efficiency for proton detection (somewhat angle dependent) is 98.9% (simulation), respectively, 98.4% (data). Also determined where the efficiencies of all three layers of the detector (from data: 94.8% (inner layer), 92.9% (middle layer), 88.1% (outer layer)). Since in this experiment the condition for neutrons was that no layer had responded, only about 0.04% of protons may be misidentified as neutrons. The probability that a neutron activates a coincidence of two layers (condition for proton) is also negligible. The TAPS veto detectors have on average an inefficiency for proton detection at the 4% level, depending on the kinetic energy. However, for TAPS additional separation of proton and neutron hits is provided by the time-of-flight *versus* energy analysis. No trace of the typical proton band was seen for "neutral" events and the possible contamination of the neutron sample with protons could be estimated at the 1% level. Cross contamination of the recoil nucleon samples was therefore negligible.

The different systematic uncertainties are summarized in table 2. It should be noted that the comparison of the quasi-free proton data to free proton data, as well as the comparison of the two different neutron analyses (see below) indicate that these estimates are pessimistic.

For the comparison of the quasi-free $\gamma p \rightarrow \eta' p$ and the $\gamma n \rightarrow \eta' n$ reactions, systematic uncertainties except the ones from the recoil nucleon detection cancel. However, these effects can be controlled in an independent way. As discussed above, the cross-section is constructed for η'-mesons in coincidence with recoil protons (σ_p), for η'-mesons in coincidence with recoil neutrons (σ_n), and for η'-mesons without any condition for recoil nucleons (σ_{np}).

Since coherent production processes are very small (see below), the cross-sections must be related by $\sigma_{np} = \sigma_n + \sigma_p$. Therefore, the neutron cross-section can be extracted in two independent ways as σ_n or as $\sigma_{np} - \sigma_p$, one depending only on neutron detection efficiency, the other depending only on proton detection efficiency. This method has been previously tested for η-photoproduction [35], where excellent agreement between the two results was found. Also for η' the two results are in good agreement, their weighted average $\langle \sigma_n \rangle$ is given as final result for the neutron cross-section and the differences between them (shown in figs. 13, 12 in sect. 5.3) are an independent estimate of the uncertainties introduced by the recoil particle detection.

4 Reaction models

In the absence of any data for polarization observables, only a preliminary interpretation of the data in the framework of reaction models, using model-dependent constraints, is possible. In 2003 Chiang *et al.* [29] have developed a reggeized model for η- and η'-production (η'-MAID), which they used to analyze the then available proton data. They parameterized contributions from nucleon resonances in the usual way in terms of Breit-Wigner curves with energy-dependent widths. Non-resonant Born terms were neglected since they were expected to be small at not too high photon energies due to the small η'-nucleon-nucleon coupling constant $g_{\eta'NN}$. However, they are included in the most recent version of the model used to fit the present data. Contributions from t-channel vector meson exchange are important and were incorporated via Regge trajectories. They found that already a model including just one S_{11}-resonance ($W = 1960\,\mathrm{MeV}$) together with the Regge trajectories could reproduce the available angular distributions for $\gamma p \to p\eta'$. Some improvement of the fit was possible by addition of a P-wave resonance, where a P_{11} or a P_{13}, both around $W = 1950\,\mathrm{MeV}$, gave equally good results. However, in the meantime, the database for the proton has been much improved and, neither the absolute magnitude nor the extreme forward-backward asymmetry of the early angular distributions [28] have been supported by the later experiments [30,17,16], so that these fits needed to be updated. For this purpose, the model was extended by addition of a D_{13}-resonance. It was then fitted simultaneously to the free proton data from CLAS and ELSA, to the present quasi-free proton data, and to the quasi-free neutron data. The effects from Fermi smearing, although not important, were taken into account for the quasi-free data sets by folding the model results with the nucleon momentum distributions.

In a different approach Nakayama and Haberzettl [31] have analyzed the first CLAS data [30]. They extended their relativistic meson-exchange model [52] for application to the $\gamma p \to p\eta'$ reaction by introducing contributions from (spin-3/2)-resonances (the earlier version considered only (spin-1/2)-states) and including energy-dependent resonance widths. In addition to the resonance contributions nucleonic s- and u-channel diagrams and, more important, mesonic t-channel contributions (ρ, ω exchange) are considered. However, due to the lack of polarization observables, they find also different solutions. In ref. [31] also the ρ- and ω-Regge trajectories have been considered instead of the t-channel rho and omega meson exchanges to describe the CLAS data [30]. There, it is found that the Regge description yields similar results as the t-channel meson exchange. Therefore, in the present work, we confine ourselves to their model with t-channel meson exchange. The "minimum" solution with the smallest number of resonances in addition to the nucleonic and mesonic currents that gives an acceptable fit includes an $S_{11}(1958)$ and $P_{11}(2104)$ as well as sub-threshold $P_{13}(1885)$ and $D_{13}(1823)$ states (which can be considered as non-resonant backgrounds). In the following, we call this solution (I), whose parameter values are summarized in table I of [31]. Solution (II) includes a further D_{13}-state at $W = 2084$ (and different parameter values for the other states as summarized in table II of [31]). In further exploratory fits (tables III–V in [31]), more resonances were added, but did not improve the fit quality significantly. Therefore, in the present work we will only discuss solution (I). A first analysis of the present quasi-free proton and neutron data was done in the following way. The results of the fits to the CLAS data for the free proton (solution (I) of [31]) have been adopted without any parameter change and folded with the momentum distribution of the bound proton, using the deuteron wave function in momentum space [53]. They are then compared to the quasi-free proton results. For the neutron, only the electromagnetic photon-resonance couplings of all states have been varied, while all other resonance parameters (position, width, decay branching ratios) have been taken from the proton fit. In a second fit, called solution (Ia), an additional S_{11}-resonance was introduced because the neutron data seems to show a broad bump at higher incident photon energies, which is not apparent for the proton. In the following, we refer to solutions (I) and (Ia) as the NH model.

5 Results

In the following all quasi-free differential cross-sections are given in the cm (center-of-momentum) system of the incident photon and a target nucleon *at rest*. Apart from the immediate threshold region, such cross-sections are only moderately smeared out by the effects of nuclear Fermi motion and can thus be compared almost directly to the corresponding results off free nucleons (see [33] for details). The angular distributions have been fitted with Legendre polynomials

$$\frac{\mathrm{d}\sigma}{\mathrm{d}\Omega} = \frac{q^\star_{\eta'}}{k^\star_\gamma} \sum_i A_i P_i(\cos(\Theta^\star_{\eta'})), \qquad (4)$$

where the A_i are expansion coefficients. The phase-space factor $q^\star_{\eta'}/k^\star_\gamma$ is also evaluated for the above cm system. The total cross-sections have been extracted from the leading Legendre coefficient A_0 of these fits. For some previous

free proton results [17,16] only angular distributions but no total cross-sections or total cross-sections extracted by integration of the angular distributions have been given. For this reason, and in order to treat all data samples in a consistent way, also for these data sets total cross-sections have been extracted in this work from the fits of the angular distributions.

5.1 Quasi-free proton cross-section

We first compare the results from the quasi-free $\gamma d \rightarrow (n)p\eta'$ reaction to free proton data. The total quasi-free cross-section off the proton is compared to free proton results in fig. 8. The angular distributions are summarized in fig. 9. Figure 8 shows also the inclusive quasi-free cross-section (σ_{np}) of single-η' production off the deuteron (no condition on recoil nucleon) and the fully inclusive cross-section (σ_x) including contributions $e.g.$ from $\eta'\pi$ final states. At the highest incident photon energies roughly 50% of the yield comes from such meson pairs. For the analysis of the single-η' channel these multiple meson production reactions have been eliminated by the condition that no further mesons have been seen in the detector and by the kinematic constraints discussed in sect. 3.1 for events where additional mesons have escaped detection.

For the comparison of the quasi-free and free proton cross-sections, one could fold the free cross-section data with the momentum distribution of the bound nucleons. However, simulations have shown that for photon energies above 1.6 GeV this effect is small compared to the uncertainty of the data. Therefore we compare the unfolded data. Apart from a few energy bins close to threshold, the shapes of the angular distributions of quasi-free and free proton data are in quite good agreement (see also fig. 12 for a comparison of the fitted Legendre coefficients). For the total cross-section, shown in fig. 8, the agreement between the present quasi-free data (blue squares) and, in particular, the recent high-precision proton data from CLAS [17] (magenta stars) is excellent. The agreement with [16] (open circles) is within the systematic uncertainties. Altogether, no important nuclear effects were observed for quasi-free η'-production off the bound proton. Therefore, we expect that quasi-free η'-photoproduction off the bound neutron is a reasonable approximation of the free neutron reaction.

## 5.2 Inclusive quasi-free cross-section

The most simple approach to estimate the behavior of the neutron cross-section is the measurement of the inclusive $\gamma d \rightarrow (np)\eta'$ reaction, where only the η' is detected, production of further mesons is excluded by the missing-mass cut, and no conditions for the detection of recoil nucleons are applied. Since coherent contributions are small, the result is the incoherent sum of quasi-free proton and quasi-free neutron cross-section.

The advantage of this approach is the comparably good statistical quality of data without detection of coincident neutrons. The angular distributions for this inclusive reaction are summarized in fig. 10 (the total cross-section σ_{np} is included in fig. 8). The angular distributions are compared to the recent CLAS data for the free proton [17], scaled up by a factor of two.

Agreement between the two data sets therefore signals regions where proton and neutron cross-sections are more or less identical. This is almost perfectly the case (sometimes with the exception of the extreme backward angles) for incident photon energies above 1.9 GeV. This is the region where the angular distributions are strongly forward peaked, which in the models is mainly attributed to the contribution of t-channel processes. At incident photon energies between 1.6–1.9 GeV, the inclusive cross-section is significantly smaller than twice the proton values, indicating a region, with $\sigma_n < \sigma_p$, which could be a first hint to different resonance contributions. For the lowest-energy bin (1475 MeV) effects of nuclear Fermi motion become important. Close to the threshold, energy conservation asymmetrically favors nucleon momenta anti-parallel to the incoming photon momentum, which results in an enhancement of meson backward angles (see [33] for details). The data are compared to fits with the NH (solution (I)) and MAID model. Shown is the incoherent sum of the model results for proton and neutron, where the neutron couplings have been fitted to the quasi-free neutron data (see next section). The agreement with the data for the other versions of the NH model, which are not shown, is similar to solution (I).
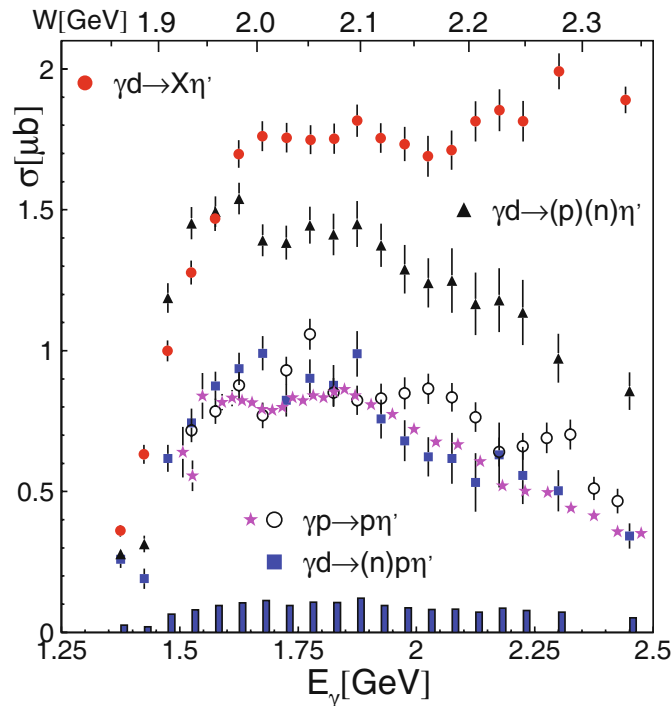
Fig. 8. (Colour on-line) Total cross-sections for total inclusive $\gamma d \rightarrow X\eta'$ (σ_x), inclusive quasi-free $\gamma d \rightarrow np\eta'$ (σ_{np}) and quasi-free proton $\gamma d \rightarrow (n)p\eta'$ (σ_p) cross-sections. The quasi-free proton cross-section is compared to the free proton results from [16] (open circles) and [17] (magenta stars). Bar histogram at the bottom: systematic uncertainty of quasi-free proton data excluding the overall normalization uncertainty.
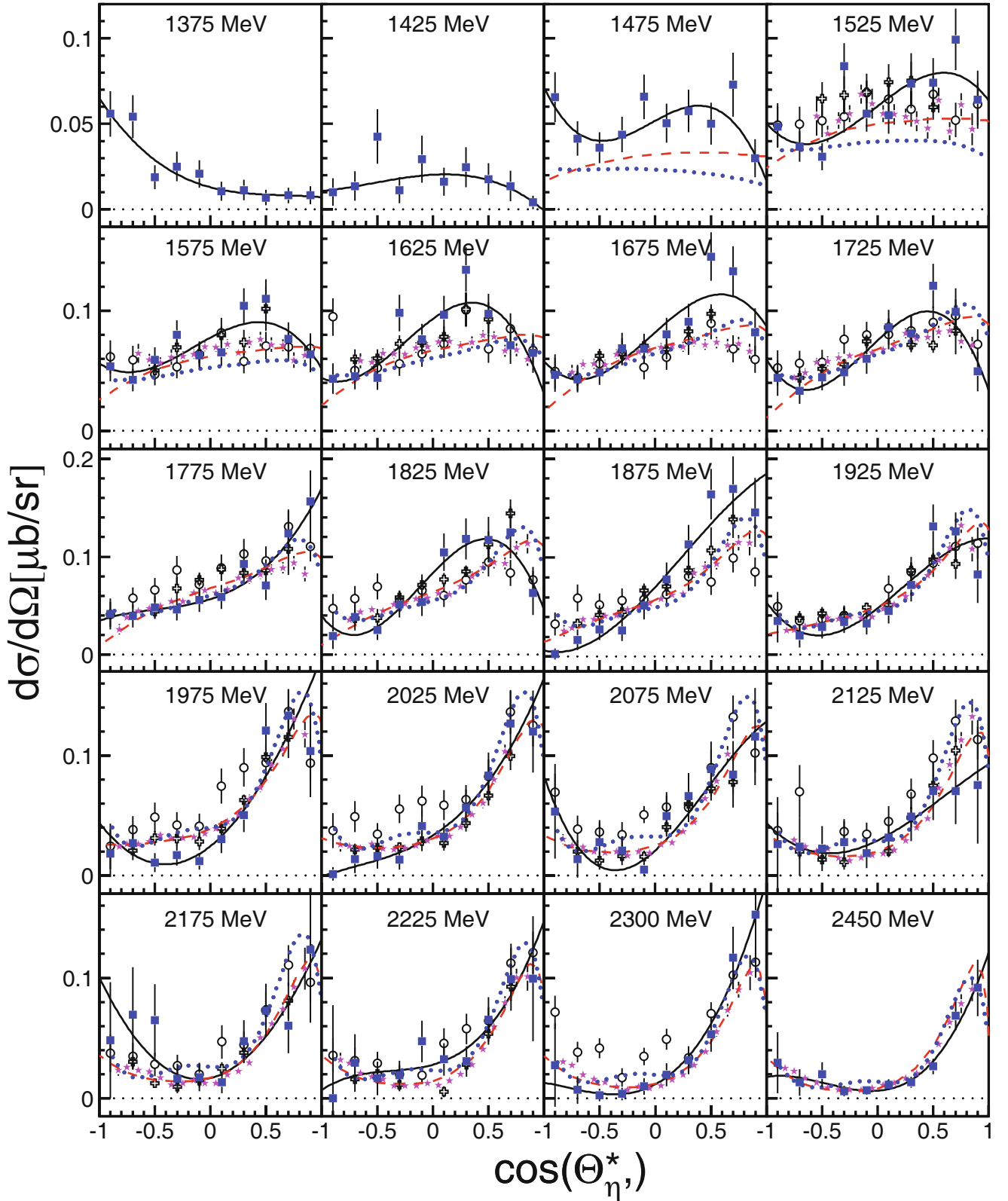
Fig. 9. (Colour on-line) Comparison of quasi-free η'-production off the bound proton ((blue) squares) to the free proton data: (black) open circles [16]; (black) open crosses: [30]; (magenta) stars: [17]. The numbers given in the figure indicate the bin centers in incident photon energy (note: the first two bins are below the free nucleon production threshold). Note: results from [30,17] correspond partly not exactly to the same energy bins as the present results. The closest bins or the average of overlapping bins have been chosen. All uncertainties are only statistical. Lines: solid (black): Legendre fits to present data; dashed (red): solution (I) of the NH model; dotted (blue): η'-MAID.
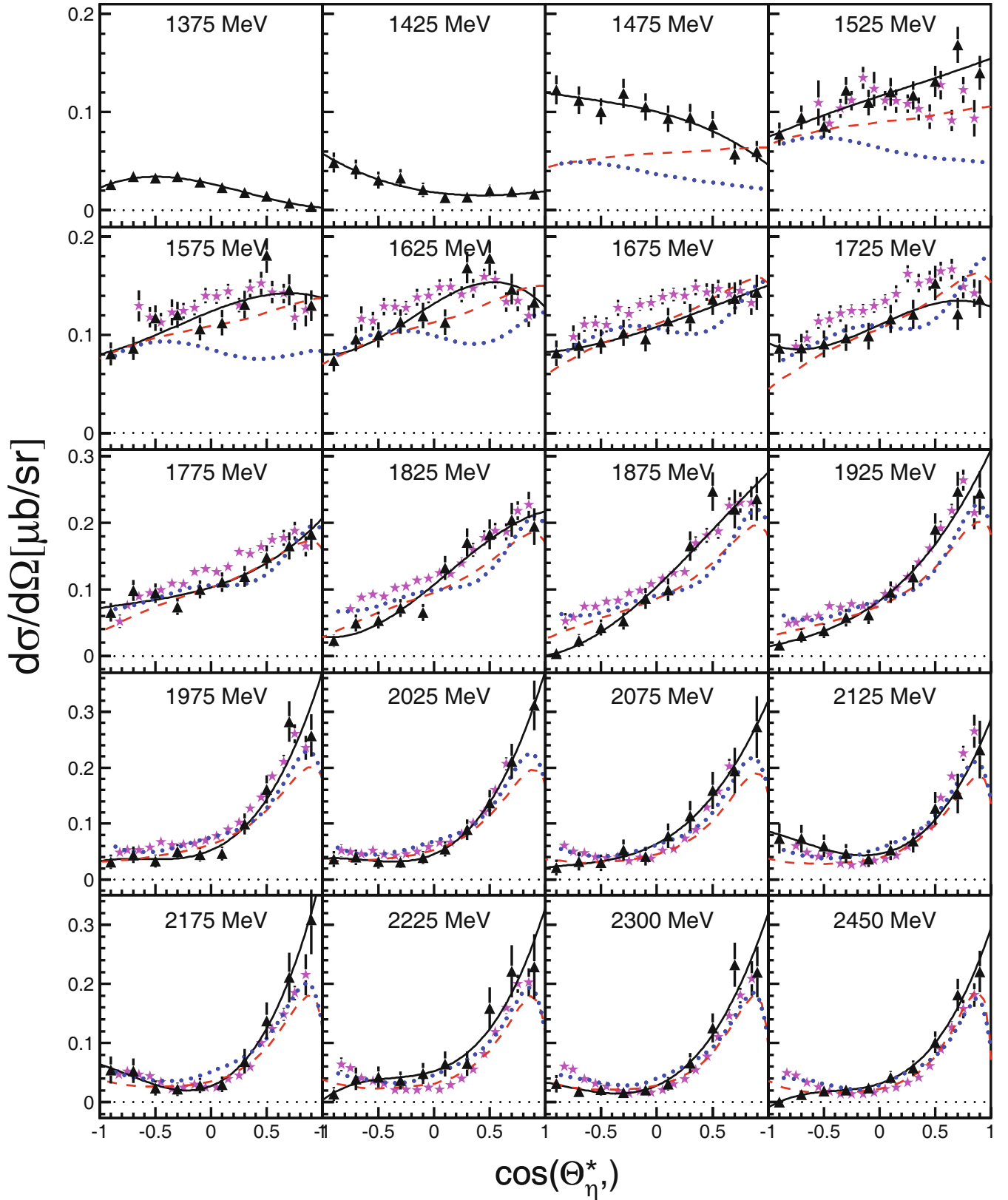
Fig. 10. (Colour on-line) Angular distributions for the inclusive quasi-free process $\gamma d \to (np)\eta'$ of single-η' production (black triangles). (Magenta) stars: the free proton results from [17] scaled up by factor of two. Note: results from [17] correspond partly not exactly to the same energy bins as the present results. The closest bins or the average of overlapping bins have been chosen. All uncertainties are only statistical. Full (black) lines: Legendre fit of present data; dashed (red) lines: solution (I) of the NH model; (blue) dotted lines: η'-MAID model.

5.3 Quasi-free neutron cross-section

As discussed in sect. 3, the quasi-free neutron cross-section can be extracted by coincident detection of the recoil neutrons or as difference of the inclusive and quasi-free proton cross-section. The two methods give similar results, the averages of the angular distributions are summarized in fig. 11. For the fitted Legendre coefficients also the two individual data sets are shown in fig. 12 as an estimate of systematic uncertainties. The total cross-section is compared in fig. 13 to the proton data and to the results from the reaction models. Differences between the two extraction methods are indicated by the bar histogram in this figure.

As expected from the discussion of the inclusive data, proton and neutron angular distributions are similar in magnitude and shape for photon energies above 1.9 GeV. However, at lower energies they are significantly different. The high-precision CLAS proton data [17] show a kind of double-bump structure in the total cross-section with shallow maxima around $W = 1975\,\mathrm{MeV}$ and $W = 2080\,\mathrm{MeV}$ (cf. fig. 8), which at the very limit of statistical significance is even reflected in the present proton and inclusive data (cf. fig. 13). The earlier free proton CLAS data [30] may also contain such structures. In fact, the model calculation of ref. [31], which fits the differential cross-sections data of ref. [30], has predicted such shallow bump structures in the total cross-section at about the same two energies.

For the neutron, the first bump is more clearly visible, while the second one is suppressed.
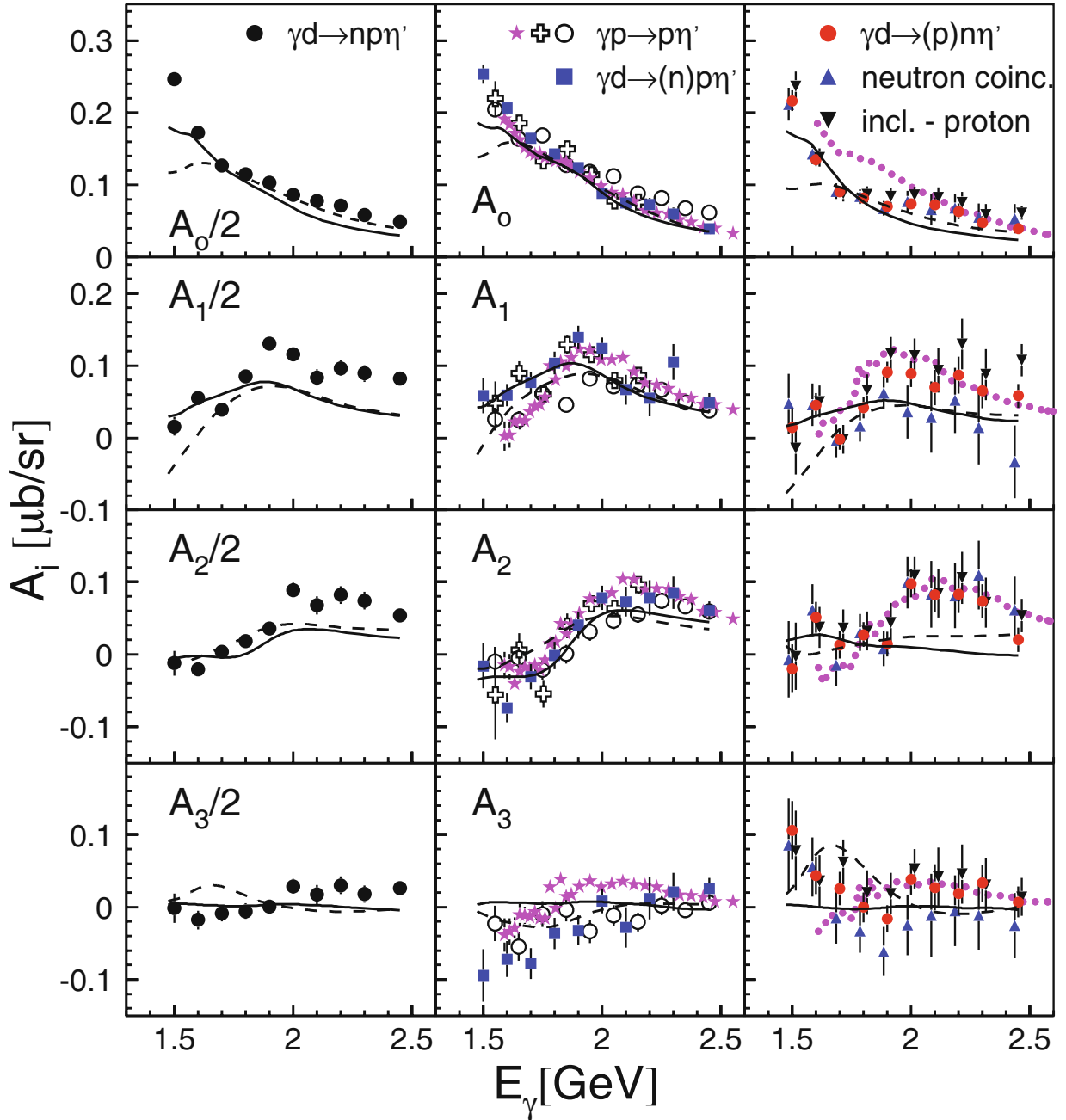
The fitted coefficients of the Legendre representation of the angular distributions are summarized in fig. 12. For the quasi-free neutron the results for the two different extraction methods and for the average are shown. The agreement of the two data sets for the even coefficients (A_0, A_2) is mostly within statistical uncertainties. Some discrepancies outside statistical uncertainties are observed for A_1 and A_3. These odd coefficients are very sensitive to the extreme forward and backward angles, where due to small detection efficiencies uncertainties in the data are more important. For the same reason no values are given for A_3 for the earlier CLAS data [30]. Due to the relatively small angular coverage the fits were not sensitive to it.

The excellent agreement between free and quasi-free proton data is demonstrated in the center column of the figure. Effects from nuclear Fermi motion are mostly insignificant. The largest effect results again for the odd coefficients (A_1, A_3) since the asymmetric preference for nucleon momenta anti-parallel to the photon momentum induces a false forward-backward asymmetry in the quasi-free data. However, the effect is small. In case of the most precise recent CLAS data, folding with Fermi motion (not shown in the figure) improves slightly the agreement for the odd coefficients. For a better comparison of proton and neutron data, the new CLAS proton data are included as magenta dotted lines into the pictures of the neutron column. The largest difference occurs for the A_0 coefficient, while the results are quite similar for the A_1, A_2, and A_3 coefficients. Only close to threshold there could be some systematic deviation.
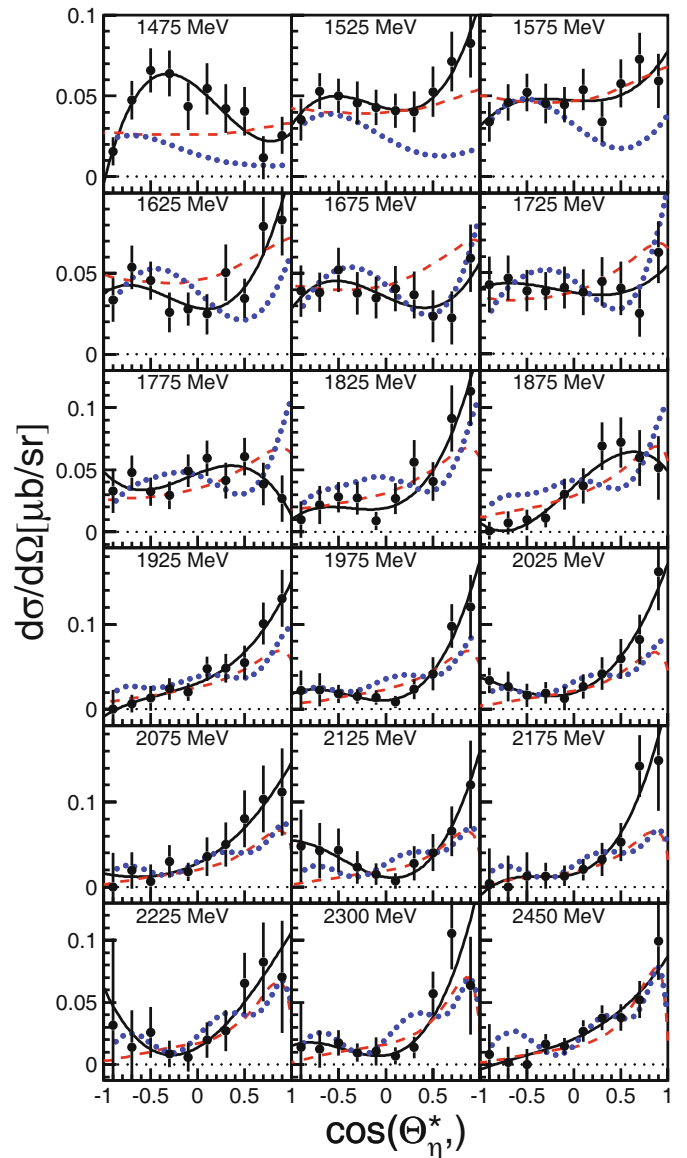
Fig. 11. (Colour on-line) Angular distributions for the quasi-free $\gamma n \to n\eta'$ reaction. Only statistical uncertainties. Solid (black) lines: Legendre fit to data. Dashed (red) lines: solution (I) of the NH model; dotted (blue) lines: η'-MAID model.

The neutron data have been fitted with the NH model solution (I) (the other solutions give very similar results) and the η'-MAID model. The results are shown in figs. 13, 11, 12. For both models, all resonance parameters except the electromagnetic neutron couplings were taken over from, respectively were dominated by, the fits to the proton data. For the NH model also a modified version with an additional S_{11}-resonance was tested, which, however did not much improve the agreement with the data. The parameters of the two models are summarized in tables 3, 4. For both models the agreement between fit and data is less good than for the proton data. For the total cross-section the MAID-fit does not well reproduce the threshold region. None of the fits reproduces the region above 2 GeV. For the coefficients of the angular distribu-

Fig. 12. (Colour on-line) Coefficients of the Legendre polynomials for the fitted angular distributions. Left-hand column: inclusive reaction scaled down by factor of 2. Center column (proton targets): quasi-free data (blue squares); free proton data: open crosses [30] (omitted for A_3), open circles [16], (magenta) stars [17]. Right-hand column (present quasi-free neutron data): (blue) upward triangles from neutron coincidence, (black) downward triangles from difference of inclusive and proton data, (red) circles from averaged data. Symbols have been slightly displaced to the left (right) for upward (downward) triangles to make the plot better readable. In all plots, solid lines: solution (I) of the NH model; dashed lines: η'-MAID; for neutron: (magenta) dotted lines are the CLAS proton data.

tions particular A_2 disagrees with the data, which like for the proton rises above 2 GeV while it is flat and very small for the fits.

In this most basic version both models include apart from the background terms an S_{11}- and a P_{11}-resonance around $W = 2$ GeV (respectively, $W = 2.1$ GeV). It must be emphasized again that in both models these solutions are by far not unique. Nevertheless, there seems to be agreement in so far, as both models need an S_{11}-resonance close to threshold in order to fit the sharp rise of the total cross-section and a P_{11}-state to explain the shape of the angular distributions via an S-P interference term, which essentially has a linear $\cos(\Theta_{\eta'}^\star)$ behavior. Although also a P_{13}-state and/or the interference with background

Table 3. Resonance parameters of the η'-MAID model [29]. Resonance positions M and total widths Γ_{tot} in MeV. Resonance couplings defined by $\chi_J^N \equiv \sqrt{\beta_{N\eta'}} A_J^N$ (in units of $10^{-3}\,\mathrm{GeV}^{-1/2}$), where $\beta_{N\eta'}$ denotes the $N^* \to N\eta'$ branching ratio and A_J^N the helicity amplitude; $N = p, n$ and $J = 1/2, 3/2$. R is the neutron/proton ratio of the electromagnetic widths: $R \equiv \Gamma_{\gamma n}/\Gamma_{\gamma p}$. Coupling constants for the background nucleon born terms $g_{\eta'NN} = -0.18$ and vector meson exchange (ρ, ω), $g_{\rho NN} = 2.0$, $\kappa_{\rho NN} = 3.5$, $g_{\omega NN} = 12.0$, $\kappa_{\omega NN} = 0.56$ (vector coupling g and tensor/vector ratio κ), $g_{\rho\eta'\gamma} = 1.24$, $g_{\omega\eta'\gamma} = -0.43$ (for details see [29]).

Resonance	M	Γ_{tot}	$\chi_{1/2}^p$	$\chi_{3/2}^p$	$\chi_{1/2}^n$	$\chi_{3/2}^n$	R
S_{11}	2004.	286.	19.7		-14.6		-0.56
P_{11}	2100.	100.	2.0		0.77		0.15
P_{13}	1920	100	-1.0	-4.2	5.0	0.97	1.4
D_{13}	2150.	230.	12.0	-5.2	-1.4	0.96	0.02

Table 4. Resonance parameters of version (I) of the NH model [31]. Notation as in table 3. Background parameters: $g_{\eta'NN} = 0.43$, $g_{\rho NN} = 3.3$, $\kappa_{\rho NN} = 6.1$, $g_{\omega NN} = 10.0$, $\kappa_{\omega NN} = 0$, $g_{\rho\eta'\gamma} = 1.25$, $g_{\omega\eta'\gamma} = 0.44$. The (spin-3/2)-resonances, P_{13} and D_{13}, are sub-threshold resonances and, as such, they may be considered as part of the background contribution. Further details of model (I) may be found in table I of ref. [31]. Version (Ia) includes in addition a second S_{11}-resonance at $W = 2180\,\mathrm{MeV}$ and $\Gamma = 110\,\mathrm{MeV}$.

Resonance	M	Γ_{tot}	$\chi_{1/2}^p$	$\chi_{3/2}^p$	$\chi_{1/2}^n$	$\chi_{3/2}^n$	R
S_{11}	1958.	139.	$-12.$		$-17.$		1.91
P_{11}	2104.	136.	$-13.$		$-5.$		0.16
P_{13}	1885.	59.					0.02
D_{13}	1823.	450.					1.24
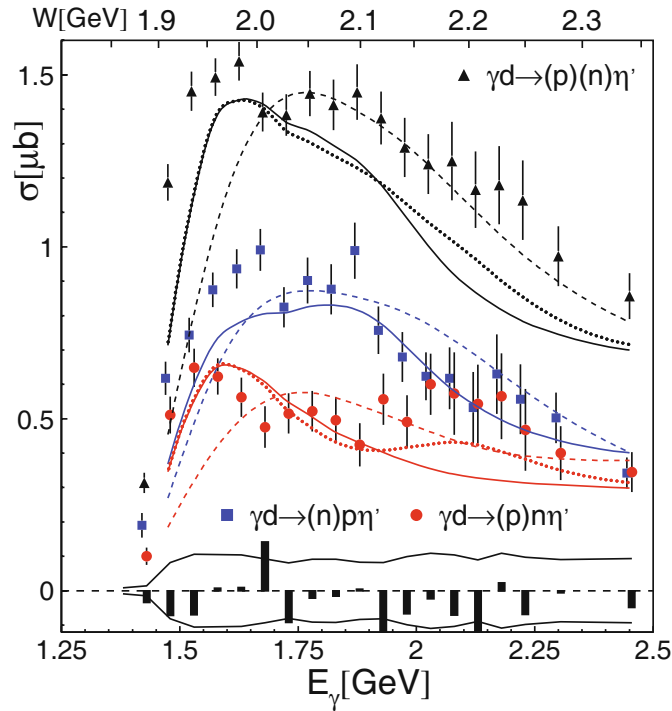
Fig. 13. Total cross-section for inclusive σ_{np}, proton σ_p, and neutron $\langle\sigma_n\rangle$ final state. Bar histograms: $(\sigma_n + \sigma_p - \sigma_{np})$, curves at bottom: $\pm$ systematic uncertainty of σ_n. Proton (neutron) data points slightly displaced to the left (right) for better readability of the figure. Curves: fits with reaction models. NH model: solid: solution (I); dotted: solution (Ia); dashed: η'-MAID.

amplitudes can give rise to such a behavior. For both states there are candidates in the Particle Data Group Review [20], the $S_{11}(2090)$ and the $P_{11}(2100)$ both one-star states with not well-defined positions and widths. In the case of the P_{11} both model analyses result in similar positions, widths, and neutron/proton ratio of the electromagnetic couplings, although the absolute contribution of this state is stronger for the NH model. The S_{11} has similar positions but different widths. In the case of the MAID model the proton coupling is stronger and there is a negative sign between proton and neutron coupling, while for the NH model the relative sign is positive and the neutron coupling is stronger. Consequently, not even for these two "dominant" resonances agreement is found between the two models. Obviously, further observables must be measured to arrive at better constraints for the model analyses.

Here, one should also note that already in the Lagrangian parameterizations of the background terms differences occur between the two models in both, the structure of some Lagrangians, as well as in the numerical values of coupling constants. As an example for the vector meson currents, the coupling constant for the t-channel ω-exchange is positive for the NH model, while it is negative for the MAID model (see tables 4, 3). On the other hand, the corresponding coupling for the ρ-meson is positive in both models. This leads to a destructive interference between this two terms in the MAID model, while the interference is constructive for the NH model. A more detailed analysis of the t-channel background terms is therefore also necessary. This might profit from data at higher inci-

dent photon energies, where this contribution dominates. Another example are the baryonic background currents where the NH model uses a pure pseudo-vector coupling at the $NN\eta'$ vertex, while MAID uses pseudo-scalar coupling, again giving rise to a relative sign between the amplitudes of the two models.

5.4 The coherent $\gamma d \rightarrow \eta' d$ reaction

Coherent photoproduction is important due to its direct connection to the iso-scalar parts of electromagnetic transition amplitudes. However, due to the dependence on the nuclear form factor it is strongly suppressed for heavier mesons. The results for the total cross-section obtained from the analysis discussed in sect. 3 are summarized in fig. 14. The typical size of systematic uncertainties can be estimated by a comparison of the results from the three analyses using more or less stringent cuts for the missing energy analysis, which is needed to remove background from quasi-free processes. All results are on the order of only a few nb, the values from the two more stringent cuts ($\Delta E_{\eta'}$ between $\pm 25\,\mathrm{MeV}$ or between -50–$0\,\mathrm{MeV}$) are in reasonable agreement, those from the most open cut ($\pm 50\,\mathrm{MeV}$) may still include a small background contribution.

The results from the re-fitted reggeized MAID model [29] discussed above have been used to model the coherent reaction, using the parameters summarized in table 3. The formalism is based on a standard impulse approximation without multiple scattering contributions, i.e. the nuclear transition operator is taken as a sum of free single nucleon operators sandwiched between the deuteron wave functions. The general expression for the nuclear amplitude reads

$$T_{M_f M_i \lambda_\gamma} = 2 \int \frac{\mathrm{d}^3 p}{(2\pi)^3} \, \psi_{M_f}^\dagger \left(\mathbf{p} - \frac{1}{2}\mathbf{q} \right) t_{\gamma\eta'}^{\lambda_\gamma} \, \psi_{M_i} \left(\mathbf{p} - \frac{1}{2}\mathbf{k} \right), \tag{5}$$

where $\mathbf{k}$ and $\mathbf{q}$ are momenta of the initial photon and a final meson. The indices M_f, M_i, and λ_γ are, respectively, the z-projection of the final and initial deuteron spin and the photon polarization index. For the deuteron wave function, $\psi_M(\mathbf{p})$, the momentum space representation

$$\psi_M(\mathbf{p}) = \sum_{L=0,2} \sum_{M_L} (1M - M_L \, L M_L | 1M) u_L(|\mathbf{p}|)$$
$$\times Y_{L M_L}(\hat{p}) \chi_{M - M_L} \tag{6}$$

is taken, with χ_m being the triplet spin wave function. For the spatial part $u_L(p)$ the parameterization [54] derived from the Bonn NN potential model was used. For η'-photoproduction details of the deuteron wave function are more important than for lighter mesons since due to the large mass already at threshold large momentum transfers are involved. This causes a strong dependence on the behavior of the nuclear potential at small distances, in particular the D-wave component of the wave function becomes important. The calculations predict that, for exam-
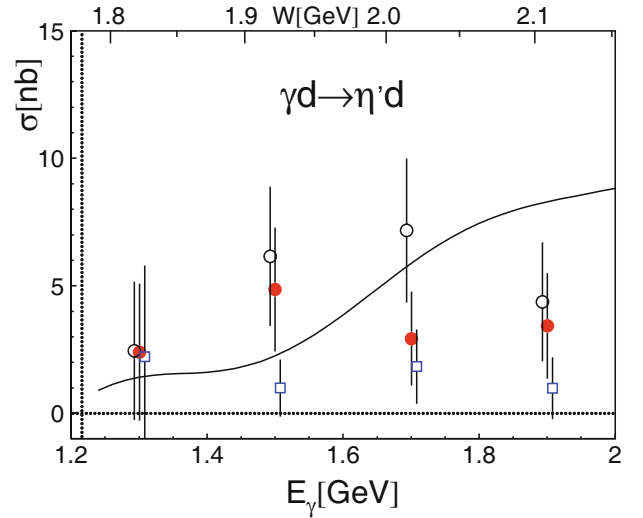
Fig. 14. (Colour on-line) Total cross-section for the coherent reaction $\gamma d \rightarrow d\eta'$. Different symbols correspond to analyses with different analysis cuts: closed (red) points: $\pm 25\,\mathrm{MeV}$ η' missing mass; open circles: $\pm 50\,\mathrm{MeV}$; open (blue) squares: -50–$0\,\mathrm{MeV}$. Solid line: model prediction using the η'-MAID multipoles.

ple at photon energies around $1.5\,\mathrm{GeV}$, the D-wave contributes already roughly 50% to the total cross-section.

The operator for η'-photoproduction on a single nucleon has the well-known spin structure in the Pauli matrix representation

$$t_{\gamma\eta'}^{\lambda_\gamma} = K_{\lambda_\gamma} + \mathbf{L}_{\lambda_\gamma} \cdot \boldsymbol{\sigma}, \tag{7}$$

with the spin-flip component $\mathbf{L}$ and the non–spin-flip K.

The result corresponding to the parameter set from table 3 is compared to the data in fig. 14. Given the simplicity of the impulse approximation, neglecting all two-body mechanisms as well as final-state interaction effects, the agreement is quite good, demonstrating that the relative contribution of iso-scalar components is well represented in the model.

The predictions for the angular dependence are very sensitive to the assumed resonance and background contributions. For example, at low incident photon energies, where the S_{11}-resonance makes a large contribution, the spin-flip amplitude $\mathbf{L}$ is dominant giving rise to a forward peaking of the cross-section. At higher incident photon energies, where other resonances and the t-channel background dominate, the spin-independent part K is strong. This part is proportional to $\sin(\Theta_{\eta'}^\star)$ and thus vanishes at forward angles. Due to the statistical limitations of the data, it was not possible to extract angular distributions. A measurement with better statistical quality is highly desirable.

6 Summary and conclusions

We have reported the first measurement of η'-mesons off the deuteron. Both, the quasi-free and the coherent reac-

tion carry important information about the iso-spin composition of the elementary reaction on the free nucleon.

For the proton case, it has been demonstrated with this experiment that the quasi-free cross-section off the bound nucleon is very similar to the free proton cross-section. No significant nuclear effects, *e.g.* from FSI processes, have been observed. At the given level of statistical precision of the data, even effects from the momentum distribution of the bound nucleons are almost insignificant. At low incident photon energies, they cause a small artificial forward-backward asymmetry in the angular distributions (coefficient A_1 in the Legendre series). At somewhat higher energies, folding the free proton cross-section with the momentum distribution improves slightly (within systematic uncertainties) the agreement of free and quasi-free data for the A_3 coefficient of the angular distributions. Only at very low incident photon energies, also the magnitude of the cross-section is affected, but in that range free nucleon results are also not available or not precise. The agreement of the quasi-free data with the most recent measurement off the free proton from the CLAS Collaboration [17] was found at a level much below the estimated systematic uncertainty of the present experiment. Consequently, the deuteron can be regarded as a very well-suited target to study the $\gamma n \to \eta' n$ reaction.

The quasi-free reaction off the bound neutron has been studied in two different ways with different sources of systematic uncertainty. In one approach, the η'-mesons were detected in coincidence with the participant neutrons. In the second approach, the cross-section obtained for coincident participant protons was subtracted from the inclusive results without condition for recoil nucleons. Since the detection efficiency for protons and neutrons is very different, a comparison of the two results gives a good estimate of the systematic uncertainty for recoil particle detection. We had previously found excellent agreement for a similar analysis of η-photoproduction [35], which used the same data set. Also for the present analysis of η'-photoproduction good agreement is found, which indicates that systematic effects are well under control. Only for the extreme forward and backward angular range, some discrepancies remain, which affect mainly the A_1 coefficient of the Legendre series for the angular distributions (see fig. 12). Altogether, the quality of the present $\gamma n \to n\eta'$ data is mostly limited by counting statistics, not so much by the systematic effects originating from the complications of a quasi-free reaction.

Proton and neutron cross-sections behave similarly at incident photon energies above 2 GeV, where contributions from t-channel exchange are important. At lower incident photon energies, in particular between 1.6 and 1.9 GeV, where the proton cross-section peaks, the behavior is different, which might point to different resonance contributions, but could also arise from changing interference terms between the resonances or between resonances and non-resonant background.

The data have been compared to two different models, both with contributions from a similar set of nucleon resonances and background terms, in particular from t-channel

mesonic currents. As already pointed out in [31] differential cross-sections alone cannot uniquely determine the contributing reaction mechanisms. Consequently, in the framework of both models different solutions can be found. Future measurements of polarization observables have to clarify the situation.

Finally, also a first estimate of the coherent $\gamma d \to d\eta'$ contribution at the level of at most a few nanobarn ($\sigma_{d\eta'} < 5\,\mathrm{nb}$ for all investigated photon energies is a reasonable estimate) has been extracted. This reaction is not only important for the iso-spin separation of the elementary production amplitudes, but aims also at the study of the η' nucleon interaction via FSI effects. The extracted results are consistent with an impulse approximation, indicating that the iso-spin composition of the model amplitudes is at least not unreasonable and that FSI contributions are not substantial. However, the statistical limitation of the data is even more important at this low cross-section level, so that effects beyond impulse approximation could not be studied.

References

1. B. Krusche, S. Schadmand, Prog. Part. Nucl. Phys. **51**, 399 (2003).
2. V.D. Burkert, T.-S. Lee, Int. J. Mod. Phys. E **13**, 1035 (2004).
3. B. Krusche *et al.*, Phys. Rev. Lett. **74**, 3736 (1995).
4. B. Krusche *et al.*, Phys. Lett. B **397**, 171 (1997).
5. J. Ajaka *et al.*, Phys. Rev. Lett. **81**, 1797 (1998).
6. A. Bock *et al.*, Phys. Rev. Lett. **81**, 534 (1998).
7. C.S. Armstrong *et al.*, Phys. Rev. D **60**, 052004 (1999).
8. R. Thompson *et al.*, Phys. Rev. Lett. **86**, 1702 (2001).
9. F. Renard *et al.*, Phys. Lett. B **528**, 215 (2002).
10. M. Dugger *et al.*, Phys. Rev. Lett. **89**, 222002 (2002).
11. V. Crede *et al.*, Phys. Rev. Lett. **94**, 012004 (2005).
12. T. Nakabayashi *et al.*, Phys. Rev. C **74**, 035202 (2006).
13. O. Bartholomy *et al.*, Eur. Phys. J. A **33**, 133 (2007).
14. D. Elsner *et al.*, Eur. Phys. J. A **33**, 147 (2007).
15. H. Denizli *et al.*, Phys. Rev. C **76**, 015204 (2007).
16. V. Crede *et al.*, Phys. Rev. C **80**, 055202 (2009).
17. M. Williams *et al.*, Phys. Rev. C **80**, 045213 (2009).
18. M. Sumihama *et al.*, Phys. Rev. C **80**, 052201(R) (2009).
19. E.F. McNicoll *et al.*, Phys. Rev. C **82**, 035208 (2010).
20. C. Amsler *et al.*, Phys. Lett. B **667**, 1 (2008).
21. J. Ajaka *et al.*, Phys. Rev. Lett. **100**, 052003 (2008).
22. E. Gutz *et al.*, Eur. Phys. J. A **35**, 291 (2008).
23. I. Horn *et al.*, Phys. Rev. Lett. **101**, 202002 (2008).

24. I. Horn *et al.*, Eur. Phys. J. A **38**, 173 (2008).
25. V.L. Kashevarov *et al.*, Eur. Phys. J. A **42**, 141 (2009).
26. E. Gutz *et al.*, Phys. Lett B **687**, 11 (2010).
27. J.F. Zhang *et al.*, Phys. Rev. C **52**, 1134 (1995).
28. R. Plötzke *et al.*, Phys. Lett. B **444**, 555 (1998).
29. W.T. Chiang *et al.*, Phys. Rev. C **68**, 045202 (2003).
30. M. Dugger *et al.*, Phys. Rev. Lett. **96**, 169905 (2006).
31. K. Nakayama, H. Haberzettl, Phys. Rev. C **73**, 045211 (2006).
32. S. Capstick, W. Roberts, Phys. Rev. D **49**, 4570 (1994); **57**, 4301 (1998); **58**, 074011 (1998).
33. B. Krusche *et al.*, Phys. Lett. B **358**, 40 (1995).
34. J. Weiss *et al.*, Eur. Phys. J. A **16**, 275 (2003).
35. I. Jaegle *et al.*, Phys. Rev. Lett. **100**, 252002 (2008).
36. V. Kuznetsov *et al.*, Phys. Lett. B **647**, 23 (2007).
37. F. Miyahara *et al.*, Prog. Theor. Phys. Suppl. **168**, 90 (2007).
38. D. Husman, W.J. Schwille, Phys. Bl. **44**, 40 (1988).
39. W. Hillert, Eur. Phys. J. A **28**, 139 (2006).
40. T. Mertens *et al.*, Eur. Phys. J. A **38**, 195 (2008).
41. D. Elsner *et al.*, Eur. Phys. J. A **39**, 373 (2009).
42. E. Aker *et al.*, Nucl. Instrum. Methods A **321**, 69 (1992).
43. R. Novotny, IEEE Trans. Nucl. Sci. **38**, 379 (1991).
44. A.R. Gabler *et al.*, Nucl. Instrum. Methods A **346**, 168 (1994).
45. G. Suft *et al.*, Nucl. Instrum. Methods A **538**, 416 (2005).
46. F. Bloch *et al.*, Eur. Phys. J. A **32**, 219 (2007).
47. R. Brun *et al.*, GEANT, Cern/DD/ee/84-1 (1986).
48. C. Zeitnitz *et al.*, *The GEANT-CALOR Interface User's Guide* (2001) `http://www.staff.uni-mainz.de/zeitnitz/Gcalor/gcalor.html`.
49. M. Lacombe *et al.*, Phys. Lett. B **101**, 139 (1981).
50. V. Hejny *et al.*, Eur. Phys. J. A **6**, 83 (1999).
51. E. Schäfer, PhD Thesis, University of Mainz (1993) unpublished.
52. K. Nakayama, H. Haberzettl, Phys. Rev. C **69**, 065212 (2004).
53. R. Machleidt, Adv. Nucl. Phys. **19**, 189 (1989).
54. R. Machleidt, K. Holinde, Ch. Elster, Phys. Rep. **149**, 1 (1987).